

Tissue Engineering

Tissue Engineering Manuscript Central: <http://mc.manuscriptcentral.com/ten>

Physical and biological characterisation of ferromagnetic fibre networks: effect of fibrin deposition on short-term *in vitro* responses of human osteoblasts

| | |
|-------------------------------|--|
| Journal: | <i>Tissue Engineering</i> |
| Manuscript ID: | TEA-2014-0211.R1 |
| Manuscript Type: | Original Article |
| Date Submitted by the Author: | n/a |
| Complete List of Authors: | Spear, Rose; University of Cambridge, Department of Engineering Srigengan, Brajith; University of Cambridge, Department of Engineering Neelakantan, Suresh; University of Cambridge, Department of Engineering Bosbach, Wolfram; University of Cambridge, Department of Engineering Brooks, Roger; Addenbrooke's Hospital, Division of Trauma & Orthopaedic Surgery Markaki, Athina; University of Cambridge, Department of Engineering |
| Keyword: | Biomedical Engineering, Bone < Tissue Engineering Applications (DO NOT select this phrase; it is a header ONLY), Metallic Scaffolds < Enabling Technologies (DO NOT select this phrase; it is a header ONLY) |
| Abstract: | <p>Ferromagnetic fibre networks have the potential to deform <i>in vivo</i> imparting therapeutic levels of strain on in-growing periprosthetic bone tissue. 444 ferritic stainless steel provides a suitable material for this application due to its ability to support cultures of human osteoblasts without eliciting undue inflammatory responses from monocytes <i>in vitro</i>. In the present paper, a 444 fibre network, containing 17 vol% fibres, has been investigated. The network architecture was obtained by applying a skeletonisation algorithm to 3D tomographic reconstructions of the fibre networks. Elastic properties were measured using low-frequency vibration testing, providing globally-averaged properties as opposed to mechanical methods which yield only local properties. The optimal region for transduction of strain to cells lies between the ferromagnetic fibres. However, cell attachment, at early time points, occurs primarily on fibre surfaces. Deposition of fibrin, a fibrous protein involved in acute inflammatory responses, can facilitate cell attachment within this optimal region at early time points. The current work compared physiological (3 and 5 g L⁻¹), and supra-physiological fibrinogen concentrations (10 g L⁻¹), using static <i>in vitro</i> seeding of human osteoblasts, to determine the effect of fibrin deposition on cell responses during the first week of cell culture. Early cell attachment within the inter-fibre spaces was observed in all fibrin-containing samples, supported by fibrin nanofibres. Fibrin deposition influenced the seeding, metabolic activity and early-stage differentiation of human osteoblasts cultured in the fibrin-containing fibre networks in a concentration-dependant manner. While initial cell attachment for networks with fibrin deposited from low physiological concentrations was similar to</p> |

1
2
3
4
5
6
7
8
9
10
11
12
13
14
15
16
17
18
19
20
21
22
23
24
25
26
27
28
29
30
31
32
33
34
35
36
37
38
39
40
41
42
43
44
45
46
47
48
49
50
51
52
53
54
55
56
57
58
59
60

| | |
|--|--|
| | <p>control samples without fibrin deposition, significantly higher HOBs attached onto high physiological and supra-physiological concentrations. Despite higher cell numbers with supra-physiological concentrations, cell metabolic activities were similar for all fibrinogen concentrations. Furthermore, cells cultured on supra-physiological concentrations exhibited lower cell differentiation as measured by alkaline phosphatase activity at early time points. Overall, the current study suggests that physiological fibrinogen concentrations would be more suitable than supra-physiological concentrations for supporting early cell activity in porous implant coatings.</p> |
| | |

SCHOLARONE™
Manuscripts

Review ONLY/ Not for Distribution

1
2
3
4
5
6
7
8 **Physical and biological characterisation of ferromagnetic fibre networks: effect of**
9
10 **fibrin deposition on short-term *in vitro* responses of human osteoblasts**
11

12
13
14 Rose L. Spear¹, Brajith Srigengan¹, Suresh Neelakantan¹, Wolfram Bosbach¹, Roger A.

15
16 Brooks² and Athina E. Markaki^{1*}
17
18
19
20
21

22
23 ¹*Department of Engineering, University of Cambridge, Trumpington Street, Cambridge, CB2*
24 *1PZ, UK,*

25
26
27
28 ²*Division of Trauma & Orthopaedic Surgery, Addenbrooke's Hospital, Hills Road, Cambridge,*
29 *CB2 2QQ, UK*

30
31
32
33 **Corresponding author. TEL.:+44-1223-766417. FAX.:+44-1223-332662. E-mail address:*
34 *am253@cam.ac.uk*
35
36
37
38
39
40
41
42
43
44
45
46
47
48
49
50
51
52
53
54
55
56
57
58
59
60

1. Introduction

Total hip replacement using porous metal implant surfaces has been widely implemented surgically for cementless fixation of femoral implants. Porous magneto-active layers, made of slender ferromagnetic fibres, bonded together at cross-over points, have been proposed for use as implant coatings due to their potential to impart mechanical strains *in vivo* to in-growing bone tissue (1, 2). Most ferromagnetic devices are contraindicated for medical resonance imaging due to risks related to movement and dislodgement (3); however, implant fixation using ferromagnetic materials is currently used in several dental systems for removable dental prostheses (4). Ferritic stainless steel grades, such as 444 and 447J1, have been approved for these magnetic attachments (5). 444 stainless steel exhibits enhanced corrosion resistance due to the inclusion of the strong carbide-forming elements, titanium and niobium (6, 7). This steel grade has significantly lower nickel content compared to 316L, the most common austenitic stainless steel used for clinical applications. 444 ferritic stainless steel has recently been shown to support the *in vitro* culture of human osteoblasts without eliciting undue inflammatory responses from monocytes (8). Additional studies using fibre networks composed of 444 ferritic stainless steel further support the ability to culture human osteoblasts (9) and human mesenchymal stem cells (10) without eliciting undue inflammatory responses from monocytes (11) on these scaffolds *in vitro*.

The rationale behind a porous magneto-active layer is to induce *in vivo* modelling of in-growing periprosthetic bone by the application of an external magnetic field of clinical magnitude. The aspect ratio (length / diameter) of fibre segments between joints represents an important controllable design parameter. When a magnetic field is applied, these fibre segments

1
2
3
4 tend to become aligned along the field direction, inducing deflections of individual fibres and
5
6 mechanical straining of any compliant matrix material filling the inter-fibre space – see Figure
7
8 1(a). Figure 1(b) shows predictions for the peak strain (2) induced within in-growing bone tissue,
9
10 as a function of the fibre segment aspect ratio, for two matrix stiffness levels, for a field strength
11
12 of 1 Tesla (typical of fields currently employed for diagnostic purposes). Since the stiffness of
13
14 granulation tissue is around 0.001 GPa (12) and that of immature bone is in the range of 0.03 to
15
16 0.1 GPa (12) and strains of ~1 millistrain (13, 14) are known to be effective in stimulating bone
17
18 growth, this plot suggests that beneficial therapeutic effects might be possible in the early stages
19
20 of healing using fields no greater than those already employed for diagnostic purposes. For a
21
22 given fibre material, the strain field in the inter-fibre space can be controlled via the fibre
23
24 segment aspect ratio and the magnitude of the imposed magnetic field. From Figure 1, it can be
25
26 inferred that networks with relatively high fibre segment aspect ratios would be more readily
27
28 deformable by the application of a magnetic field. An important issue in this context is that high
29
30 porosity is expected to lead to reductions in mechanical properties. Depending on the fibre
31
32 volume fraction, the network architecture (isotropic or highly-oriented), the fibre segment aspect
33
34 ratio, experimentally measured Young's moduli values are no higher than a few GPa (15-19).
35
36
37
38
39
40
41

42 The elastic properties of highly porous materials are most commonly measured using
43
44 conventional mechanical (static) testing with the majority of studies focusing on compressive
45
46 testing as it is easier to carry out compared to tensile testing or even bending. However, it is well
47
48 known that in highly porous materials inelastic straining commonly occurs at low applied loads.
49
50 Dynamic methods, on the other hand, such as vibration and ultrasonic testing, involve much
51
52 lower applied loads than conventional static methods and therefore have the potential to give fast
53
54 and accurate low-strain amplitude measure of the elastic properties. Furthermore, static methods
55
56
57
58
59
60

1
2
3 typically utilise small test specimens yielding only local properties whereas dynamic methods
4
5 can provide globally-averaged properties. Correct selection of the most appropriate method
6
7 depends on the type of materials to be investigated, their shape and the practical difficulties
8
9 associated with each of the above methods (20). For instance, in vibration, specimen shape is
10
11 important as it determines the ease with which different vibrational modes are excited. It is also
12
13 important that the wavelength of the ultrasonic wave is much greater than the scale of the
14
15 inhomogeneity in the porous material. Very “lossy” materials may be unsuitable for ultrasonic
16
17 testing as it will be hard to obtain a strong ultrasonic transmission, in which case static testing
18
19 may be more appropriate. For highly porous metallic networks of the type investigated in this
20
21 study, the elastic properties were determined with good accuracy using vibration testing.
22
23
24
25
26
27

28 When cells migrate into porous fibre networks, they initially attach to the fibre surface
29
30 and junction regions – see [image in Figure 2\(c\) from day 1 of the current study](#). Depending on
31
32 the seeding density, filling the inter-fibre space could take a few weeks (9). Deposition of fibrous
33
34 proteins may contribute to attachment of cells within the inter-fibre spaces and thus influence the
35
36 transduction of strain to cells within the networks. Fibrin is produced from fibrinopeptide chains
37
38 during acute-stage inflammatory responses due to enzymatic lysis of fibrinogen by thrombin (21-
39
40 23). It is a natural, biodegradable fibrous protein commonly used for clinical and experimental
41
42 tissue engineering applications (24), including surgical tissue adhesives (25), delivery of growth
43
44 factors (26), genes (27) and cells (28) as well as tissue engineering for cartilage (29, 30), skin
45
46 (31) and bone (32-34). The deposition of fibrin at early time-points during physiological
47
48 responses to implantation coupled with its wide-spread acceptance in clinical and tissue
49
50 engineering applications recommend this natural biopolymer for *in vitro* studies with ferritic
51
52 fibre networks.
53
54
55
56
57
58
59
60

1
2
3
4
5
6
7
8
9
10
11
12
13
14
15
16
17
18
19
20
21
22
23
24
25
26
27
28
29
30
31
32
33
34
35
36
37
38
39
40
41
42
43
44
45
46
47
48
49
50
51
52
53
54
55
56
57
58
59
60

Physiological plasma concentrations of fibrinogen fall within the range of 1.5 and 5 g L⁻¹ (35-37). Concentrations above 5 g L⁻¹ have been used for tissue engineering and cell delivery applications (28, 33, 38, 39), while higher concentrations of 50 to 115 g L⁻¹ have been used in clinical sealants (25). The majority of studies on the effects of fibrinogen concentration on cell responses have focused on concentrations above 5 g L⁻¹ (38-40) with few focused on physiological concentrations (41, 42). The results of these studies consistently demonstrated a negative correlation between cell activity and fibrinogen concentration (38, 39, 41).

In the present work, physiological fibrinogen concentrations were compared with supra-physiological concentrations, using static *in vitro* seeding of human osteoblasts, in order to determine the effect of fibrin deposition on cells infiltrating within the porous ferromagnetic fibre networks. The hypothesis was that fibrin deposition would facilitate early cell attachment within the inter-fibre spaces. Network architecture was characterised using X-ray nanotomography and in-plane network elastic constants (Young's moduli and Poisson's ratios) were measured using low-frequency vibration testing. Cell attachment, proliferation, metabolic activity and early-stage differentiation in the networks were examined for one week following fibrin deposition.

2. Materials and methods

2.1 Sintered fibre networks

Fibre network plates (Nikko Techno Ltd, Japan) were made from AISI 444, a ferritic stainless steel. The chemical composition in weight percent (wt %) is given in Table I. Typical fibre distribution and surface morphology are illustrated in the scanning electron micrographs of Figures 2(a) and 2(b). The fibre networks were manufactured by shaving 80 µm fibres off a 100

1
2
3 μm thick sheet, hence the rectangular fibre shape shown in Figure 2(b). The fibres had an
4 average length of 165 mm and occupied 17 vol%. The fibres were randomly laid to form a sheet,
5
6
7
8 compressed and bonded together at cross-over points by solid-state sintering. Fibre networks
9
10 were supplied as flat sheets with thicknesses of 1, 2 and 5 mm. Based on our previous study (15)
11
12 on solid-state sintered 316L fibre networks, it is was found that, for a given fibre volume
13
14 fraction, the network stiffnesses were comparable, irrespective of the thickness of the sheets,
15
16 suggesting that there were no significant architectural differences between the different sheet
17
18 thicknesses. For cell culture, 10 mm (± 0.5) diameter discs we cut out from the 1 mm thick
19
20 sheets using a punch press. The discs were ultrasonically cleaned for 15 min in a sequence of
21
22 acetone, ethanol and distilled water. Samples were dried at 60°C for 1 h and then sterilised by
23
24
25
26
27 dry heat at 160°C for 2 h.

2.2 Fibre network architecture

32
33 The procedure for extracting architectural parameters from the networks by means of X-
34
35 ray tomography has been described in detail elsewhere (15, 43).
36

37
38 In this study, two 444 samples were electro-discharge machined (EDM) from the network
39
40 plates into 5 mm cubes. Tomography scans, with a 7 μm spatial resolution, were acquired using a
41
42 General Electric Phoenix X-ray Nanotom system (GE Sensing & Inspection Technologies
43
44 GmbH, München, Germany) equipped with a sub-micron focal spot X-ray source. The samples
45
46 were rotated at angular increments of 0.25°, through 360°. To avoid edge effects, a sub-volume
47
48 of $4 \times 4 \times 4 \text{ mm}^3$ was analysed. Segmentation (i.e. identification of the different phases) of the
49
50 tomography scans was achieved by indicator kriging (44) which is a local, spatially adaptive
51
52 thresholding algorithm. During image segmentation, each voxel in the grey-scale tomography
53
54 scans is assigned to either the fibre phase or the air (inter-fibre space) phase. The output of the
55
56
57
58
59
60

1
2
3 segmentation procedure is a stack of binary images featuring only those two phases. The
4
5 indicator kriging algorithm was calibrated using the fibre volume fractions obtained from a
6
7 volumetric technique (weight and sample dimensions) and a density value of 7.76 Mg m^{-3} for
8
9
10 444. The reconstructed 3D fibres were then reduced to their medial axes using a skeletisation
11
12 algorithm known as 3D Medial Axis (3DMA) algorithm (Nihon Visual Science Inc., Japan) (44-
13
14 46). The medial axis is essentially a network of “one-dimensional” paths and nodes at path
15
16 intersections. This network is topologically identical to that of the fibre networks. Once the path
17
18 and nodes are defined, the number of fibre segments (sections between the joints) and the mean
19
20 segment length can be determined. It should be noted that in the context of the fibre networks, a
21
22 “fibre” is different from a “fibre segment”, i.e. a single fibre can contain a number of fibre
23
24 segments as fibres meet at intersections. The 3DMA algorithm determines the local fibre
25
26 orientations by computing the diagonalised inertia tensor of the reconstructed fibres. The three
27
28 values (eigenvalues) correspond to the moments of inertia about the principal axes. While the
29
30 eigenvectors (the axes within which the eigenvalues are defined) denote the principal directions
31
32 of orientation. For a fibre with a rectangular cross-section, the smallest eigenvalue corresponds
33
34 to the fibre axis and the associated eigenvector provides information on the fibre orientation.
35
36
37
38
39
40
41
42

43 **2.3 Network elastic properties (Plate vibration testing)**

44
45
46 The in-plane elastic constants of the network plates were determined by measuring the
47
48 vibrational resonance modes of fibre network plates with free boundaries. Using thin-plate
49
50 bending theory, detailed in (47), the measured mode frequencies, together with the plate
51
52 dimensions and density, were used to estimate the constants D_1 , D_2 , D_3 and D_4 of the plate (D_1
53
54 and D_3 are associated with bending of the plate middle surface, D_2 with Poisson’s ratio coupling
55
56
57
58
59
60

between the in-plane directions, and D_4 with out-of-plane twisting of the middle surface). After using an iterative process (47) to improve the accuracy of these constants, the in-plane elastic constants were determined using the following relationships

$$\begin{aligned}
 D_1 &= \frac{E_x}{12(1-\nu_{xy}\nu_{yx})}, \quad D_3 = \frac{E_y}{12(1-\nu_{xy}\nu_{yx})} \\
 D_2 &= \frac{\nu_{xy}E_y}{6(1-\nu_{xy}\nu_{yx})} = \frac{\nu_{yx}E_x}{6(1-\nu_{xy}\nu_{yx})} \\
 D_4 &= G_{xy} / 3
 \end{aligned} \tag{1}$$

where E_x , E_y are Young's moduli in the x - and y -directions (in-plane directions), respectively, G_{xy} , is the shear modulus in the x - y plane, and ν_{xy} and ν_{yx} are the in-plane Poisson's ratios. The detailed procedure followed to obtain the elastic constants for fibre network plates can be found elsewhere (15).

The experimental set-up used to measure the resonant frequencies involved a loudspeaker driven by a sine-wave generator, an amplifier and a standard frequency counter. The network plate was supported over the loudspeaker, mounted beneath a large flat surface, on small blocks of soft polymeric foam. It is essential to place these foam supports underneath the nodal lines of the anticipated mode. The frequency (within a range of 50 – 300 Hz, read from the frequency counter) of the sine wave was carefully tuned until the desired vibration mode was observed. This was visualised by sprinkling powder over the surface of the plate and observing the powder accumulating along the nodal lines (i.e. lines where the amplitude of vibration is zero). Sketches of some of the measured mode shapes are shown in Table II. 2 mm thick network plates were cut into square ($140 \times 140 \text{ mm}^2$) and rectangular ($140 \times 175 \text{ mm}^2$) shapes, with respective densities of 1249 kg m^{-3} and 1189 kg m^{-3} .

3. *In vitro* cell culture

3.1 Sourcing and culture of cells

All cell culture reagents were obtained from Invitrogen (Paisley, UK) and all other chemicals from Sigma (Poole, UK) except where indicated.

Human osteoblasts (HObS, 406-05f), were obtained from the European Collection of Cell Cultures. HObS were maintained in growth medium composed of McCoy's medium supplemented with 10% (v/v) foetal bovine serum (FBS), 1% (v/v) penicillin–streptomycin (10^4 units mL^{-1} penicillin and 10 g L^{-1} streptomycin) and $30 \mu\text{g mL}^{-1}$ of vitamin C (Wako GmbH, Germany). Cultures were incubated at 37°C in a humidified atmosphere containing 5% CO_2 and the medium was replaced every 2-3 days. When cultures reached 80% confluence, cells were detached from the culture flask using TrypLE[®] for further subculture. Cells from the fifth passage were used for all experiments.

3.2 Fibrin deposition

Thrombin was prepared under aseptic conditions as a $0.025 \text{ U } \mu\text{L}^{-1}$ solution in Dulbecco's phosphate buffer solution (DPBS) and frozen at -20°C until seeding. Before seeding, the fibre networks were wetted with growth medium (1 h, 20°C). Samples were placed on a sterile, hydrophobic polytetrafluoroethylene (PTFE) filter membrane (Merck Millipore, UK) to prevent droplet spreading. Fibrinogen and thrombin solutions were prepared under aseptic conditions in sterile vials respectively to each fibrinogen concentration (3, 5 or 10 g L^{-1}) or thrombin concentration (0.1 U per mg fibrinogen) using growth medium (37°C). A $50 \mu\text{L}$ droplet of fibrinogen solution was added to each fibre network sample, followed by a $50 \mu\text{L}$ droplet of

1
2
3 thrombin solution. Medium (100 μ L) without fibrinogen or thrombin was added to control
4
5 networks. The solutions were mixed by pipetting and incubated for 1 h at 37°C in an atmosphere
6
7 of 5% CO₂ in air to allow for fibrinogen lysis and fibrin deposition in the networks.
8
9

10 11 **3.3 Cell seeding**

12
13
14 Cell seeding was carried out 1 h after fibrin deposition on a sterile PTFE filter membrane
15
16 (Merck Millipore, UK) to prevent droplet spreading. Cells (5×10^4 cells per network) were
17
18 added to the fibre networks in a 100 μ L droplet of growth medium and mixed gently by
19
20 pipetting. The samples were incubated for 4 h at 37°C in an atmosphere of 5% CO₂ in air to
21
22 allow for cell attachment. After this period, samples were transferred to individual wells in a 24-
23
24 well untreated polystyrene culture plate and growth medium (1 mL) was added to each well.
25
26 Samples were incubated at 37°C in an atmosphere of 5% CO₂ in air for the specified culture
27
28 times.
29
30
31
32

33 34 35 **3.4 Morphology and distribution of fibrin**

36
37
38 Optical microscopy, scanning electron microscopy (SEM) and confocal laser scanning
39
40 microscopy (CLSM) were used to [qualitatively](#) investigate fibrin morphology and attachment to
41
42 the fibre networks. For optical and scanning electron microscopy, samples were washed twice
43
44 with DPBS, fixed for 1 h at 20°C in 3% (v/v) glutaraldehyde: 1% formaldehyde solution in
45
46 DPBS, washed three times with DPBS and dehydrated in graded series of ethanol (70%, 85%,
47
48 95% and 100%). Samples were dried using hexamethyldisilazane. [For optical microscopy,](#)
49
50 [samples were placed on a glass slide with top face upwards](#) and imaged using the dark-field
51
52 mode on a Leica DMLM upright microscope equipped [with an EC3 camera and an Application](#)
53
54 [suite V3 imaging software.](#) The images were processed in Fiji imaging software to change from
55
56
57
58
59
60

1
2
3 colour to black and white. Then, for SEM imaging, the samples were mounted on aluminium
4 stubs with carbon tape, gold coated (2.4 kV, 90s) and observed under a Zeiss Evo MA 15
5 scanning electron microscope. The numbers and diameters of fibrin nanofibres were
6 approximated in Fiji imaging software using top-view SEM micrographs such as those in Figure
7 4 (d) – (f).
8
9
10
11
12
13
14
15

16 For CLSM imaging of fibrin, fibrinogen solutions for each concentration were
17 supplemented with 1% v/v Alexa Fluor[®] 594 human fibrinogen solution in growth medium (1 g
18 L⁻¹). Samples lacking Alexa Fluor[®] 594 were used as a control for background fluorescence.
19 Samples were washed once with DPBS, fixed with 4% (w/v) formaldehyde in PBS (Affymetrix,
20 High Wycombe, UK) (10 min, 20°C), washed twice with DPBS solution and imaged using a
21 Leica SP2-UV0351/356 confocal microscope after one day of culture. Sequential z-stacks were
22 imaged for individual wavelengths and reconstructed as max z-projections using Fiji imaging
23 software. Z-projections for each wavelength were overlaid and scale bars were added to produce
24 the final image.
25
26
27
28
29
30
31
32
33
34
35
36
37

38 **3.5 Morphology and distribution of HObs**

39
40
41 CLSM of HObs enabled observation of cell morphology and distribution in the fibre
42 networks. Samples were washed once with DPBS, fixed with 4% (w/v) formaldehyde in PBS
43 (Affymetrix, High Wycombe, UK) (10 min, 20°C), washed twice with DPBS solution and
44 permeabilised (10 min, 6°C) in pH 7.2 buffer composed of sucrose (10.3 g), sodium chloride
45 (0.292 g), magnesium chloride (0.06 g), 4-(2-hydroxyethyl)-1-piperazineethanesulfonic acid
46 (HEPES) buffer (0.476 g) and Triton-X (0.5 mL) in distilled water (100 mL). Samples were
47 incubated with 5% (v/v) goat serum albumin (GSA) in DPBS (30 min, 20°C) to block non-
48
49
50
51
52
53
54
55
56
57
58
59
60

1
2
3 specific binding, washed twice with DPBS and incubated with Alexa Fluor[®] 488 phalloidin (1 h,
4 20°C), using a 1:100 dilution in DPBS. Samples were washed three times with 0.05% tween-20
5 in DPBS, mounted with slowfade[®] gold antifade mountant containing 4',6-diamidino-2-
6 phenylindole (DAPI) and imaged using a Leica SP2-UV0351/356 confocal microscope. CLSM
7 images were analysed in Fiji as mentioned before to a maximum depth of 155 µm.
8
9
10
11
12
13
14
15

16 3.6 Cell proliferation and metabolic activity

17
18 The CyQuant[®] assay for deoxyribonucleic acid (DNA) was used according to the
19 manufacturer's instructions to determine cell number at each time point (days 1, 3 and 7). After
20 aspirating the medium, the samples ($n = 3$) were washed once with DPBS and frozen at -80°C
21 until measurement. After thawing samples, CyQuant[®] lysis solution containing ribonuclease
22 (RNase) (1.35 Kunitz units/mL) was added to each sample and the solution was agitated for 1 h.
23 CyQuant[®] dye was added to 50 µL aliquots of the cell lysate and the DNA content was measured
24 fluorimetrically (excitation 485 nm, emission 520 nm) on a Fluostar Optima multidetection
25 microplate reader (BMG Labtech, Offenburg, Germany). A reference standard curve of known
26 cell number versus fluorescence was prepared for each assay, using cell aliquots that were
27 counted and frozen on the day of seeding and stored at -80°C, in order to convert the measured
28 fluorescence values into cell numbers.
29
30
31
32
33
34
35
36
37
38
39
40
41
42
43
44
45

46 The alamarBlue[®] assay (Serotec, Oxford, UK) was used to measure cell viability by
47 quantification of intracellular metabolic activity at each time point (days 1, 3 and 7). Samples (n
48 = 3) were incubated for 4 h with fresh growth medium (37°C) supplemented with 10% (v/v)
49 alamarBlue[®] reagent. Following incubation, 100 µL medium from each well was transferred in
50 triplicate to a black 96-well microplate. Fluorescence (excitation 544 nm, emission 590 nm) was
51
52
53
54
55
56
57
58
59
60

measured using the Fluostar Optima microplate reader. The percent reduction of alamarBlue[®] was calculated using the following formula (48)

$$\% \text{ reduction of alamarBlue}^{\circledR} = \frac{S_{AB}^x - S_{AB}^{\text{control}}}{S_{AB}^{100\% \text{ reduced}} - S_{AB}^{\text{control}}} \quad (2)$$

where S_{AB}^x was the alamarBlue[®] fluorescence signal of the sample at day x , $S_{AB}^{100\% \text{ reduced}}$ is the signal of the 100% reduced form of alamarBlue[®] and S_{AB}^{control} is the signal from the control solution containing the culture medium supplemented with 10% alamarBlue[®] dye. The 100% reduced form of alamarBlue[®] was produced by autoclaving (15 min, 121°C) the negative control solution.

3.7 Statistical analysis

Averages of three independent experiments, with three tested samples per fibrin concentration, were expressed as the arithmetic mean \pm standard deviation (SD). Data were analysed for homogeneity of variance with Levene's test. Data with homogenous variance were analysed for statistical significance by two-way analysis of variance (ANOVA), followed by Tukey's post-hoc test for multiple comparisons based on concentration and time. Data without homogenous variance were analysed for statistical significance using the Games-Howell post-hoc test. Differences were considered statistically significant at p values of < 0.05 .

4. Results

4.1 Network architecture

Figure 3(a) shows a tomographic reconstruction of the 444 network. By reducing the fibres to their medial axes (Figure 3(b)), the local fibre orientations and other architectural characteristics, such as the fibre segment lengths, can be extracted. The results obtained from both samples analysed are summarised in Table III. The fibre inclination angle θ stands for the angle between the fibre axis and the through-thickness direction. Figure 3(c) shows a histogram of the fibre inclination angle showing the probability

$$P(\theta_i) = \frac{1}{\Delta\theta_i} \cdot \frac{N_{\theta_i}}{\sum_i^n N_{\theta_i}} \quad (3)$$

for a fibre segment to lie at an angle of θ_i , where N_{θ_i} is the number of fibre segments falling into a bin of width of $\Delta\theta_i$, centred at θ_i . It can be seen that the majority of fibres are lying in-plane (*i.e.* at high inclination angles θ).

4.2 Network elastic properties

The measured resonant frequencies for rectangular and square network plates are shown in Table II. The resonant frequencies for the first three mode shapes (Table II), obtained using a rectangular plate, lead to first estimates of D_1 , D_3 and D_4 . To estimate D_2 , the square plate (with adjusted aspect ratio (47)) was used to observe the “X” and “O” (ring) vibration mode frequencies (mode Nos. 4 and 5 in Table II). The accuracy of these first estimates of D_1 , D_2 , D_3 and D_4 , was improved using an iterative method (47), employing numerical calculations of plate frequencies based on the Rayleigh-Ritz method. Since there should be no preferred in-plane direction in the fibre network material, this iterative process was carried out assuming in-plane transverse isotropy. The final iterated values of the four constants were used to obtain predictions

1
2
3 of mode frequencies for the two shapes of plate (only the dimensions were changed). This
4
5 resulted in considerable redundancy in the comparison. Many more modes, apart from the ones
6
7 shown in Table II, were examined in order to get a best fit of the plate's four bending constants
8
9 to the pattern of measured natural frequencies. It can be seen, for the low-frequency modes of
10
11 both plate shapes in Table II, that the general pattern of measured frequencies fits the predictions
12
13 well enough that one can have some confidence in the fitted bending constants, interpreted in an
14
15 averaged sense over the areas of both plates and over all directions of wave propagation. The
16
17 iterated and adjusted final $D_1 - D_4$ values were related to the in-plane engineering elastic
18
19 constants (E_x , E_y , ν_{xy} , ν_{yx} and G_{xy}) via Eq. (1). The elastic constants are summarised in Table
20
21 IV. It can be seen that the moduli values are similar in the in-plane directions suggesting that the
22
23 network exhibits transverse isotropy.
24
25
26
27
28
29

30 31 **4.3 Morphology and distribution of fibrin**

32
33
34 Figures 4 (a)-(c) show optical scanning electron images of the top surfaces of stainless
35
36 steel fibre networks containing fibrin. It can be seen that fibrin (multi-shaded material (grey)
37
38 between and on top of metal fibres) was deposited over the surface of the fibre networks for all
39
40 concentrations. No observable differences between the fibrin concentrations were noticed. The
41
42 nanofibrous composition of this material was confirmed by high magnification SEM images such
43
44 as those in Figure 4 (f) – (h). An estimate of the average diameter of the fibrin nanofibres,
45
46 obtained from such images, was ~90 nm (over 50 fibres per concentration were measured) for all
47
48 fibrinogen concentrations. While the diameter of the nanofibres remained constant with
49
50 increasing fibrinogen concentration, the number of fibrin nanofibres per unit of surface area
51
52
53
54
55
56
57
58
59
60

1
2
3 increased, contributing to a decrease in the pore space between the fibrin nanofibres,
4
5 qualitatively observed using SEM images such as those illustrated in Fig. 4 (f) – (h).
6
7

8
9 The deposition of fibrin, rather than cell deposition of collagen, was confirmed by
10
11 qualitative analysis of CLSM images similar to the insert in Figure 4(b), showing the top view of
12
13 a fibre network containing fibrin supplemented with 1% fluorescently-labelled fibrin. Fibrin
14
15 deposition (red fluorescence) was observed over and between the metal fibres (observed as grey
16
17 in reflectance mode).
18
19

20 21 22 **4.4 Morphology and distribution of HObs** 23

24
25 Figure 5 shows representative fluorescence images of HObs following 1 and 7 days of
26
27 culture. Comparison of control networks without fibrin (Figures 5 (a, e, i, m)) and fibrin-
28
29 containing networks (Figures 5 (b-d), (f-h), (j-l) and (n-p)) indicated noticeable differences in the
30
31 HOb attachment pattern. For control samples without fibrin, cells with well-spread morphologies
32
33 were observed only on the metallic fibre surfaces and junctions as shown in Figures 5 (a, e, i, m).
34
35 This association of the cells solely with the metallic fibres for the control samples continued
36
37 throughout the duration of the study as indicated by Figure 5(i). In contrast, all of the fibrin-
38
39 containing samples showed cell attachment over and between the fibres throughout the duration
40
41 of the study (Figures 5 (b-d), (f-h), (j-l) and (n-p)). For all samples, the observed number of
42
43 HObs increased between days 1 and 7.
44
45
46
47
48

49
50 Representative SEM images of the top surface of the fibre networks, following fibrin
51
52 deposition and cell culture for 7 days, are shown in Figure 6. For all fibrin-containing samples,
53
54 fibrin nanofibres, confirmed by fluorescence images (see insert in Figure 4(b)), were observed
55
56 beneath the cell bodies and cytoplasmic projections in high magnification images (Figure 6).
57
58
59
60

4.5 Cell proliferation and metabolic activity

Figure 7(a) shows the number of HObs measured by CyQuant[®] DNA analysis of the samples following 1, 3 and 7 days of culture. Significantly higher cell numbers were measured on the supra-physiological (10 g L⁻¹) and high physiological (5 g L⁻¹) concentrations of fibrin compared to networks with control samples without fibrin. Furthermore, significantly higher numbers of cells were measured on supra-physiological concentrations compared with low physiological concentrations. For all networks, there was a significant increase in the numbers of HObs between 1 and 7 days of culture. Figure 7(b) shows the number of cells attached to each sample as a percent of the initial seeding concentration. The results show a significant positive correlation between fibrin concentration and the percent of HObs seeded on the networks.

Figure 7(c) shows the metabolic activity of HObs as measured by the reduction of alamarBlue[®] reagent. Cells cultured on physiological (3 and 5 g L⁻¹) concentrations had significantly higher metabolic activity than control samples without fibrin after 1 day in culture. No significant differences were measured between cells cultured on supra-physiological concentrations and other concentrations. After 3 days of culture, HObs cultured on low physiological concentrations (3 g L⁻¹) also had significantly higher metabolic activity compared to the control samples, while supra-physiological and high physiological concentrations were statistically similar to control samples.

5. Discussion

The current work presents the first study concerning the effect of fibrin nanofibre deposition on *in vitro* responses of HObs to porous networks composed of 444 ferromagnetic stainless steel fibres. These ferromagnetic fibre networks have been proposed as a bone

1
2
3 regeneration scaffold designed to induce *in vivo* modelling of in-growing periprosthetic bone by
4 the application of an external magnetic field of clinical magnitude. The present study builds upon
5 earlier work with these stainless steel grades in fully-dense form (8) and as fibre networks (9,
6 11). These earlier studies established the suitability of these fibre networks for *in vitro* cell
7 culture with a range of different cell types, including human mesenchymal stem cells and
8 osteoblasts. It was observed that cell attachment at early time points was associated solely with
9 the surfaces and junctions of the metal fibres (9, 11). Similar findings were observed in the
10 networks used in the present study as illustrated in Figure 2(c). However, theoretically the
11 optimal region for transduction of strain to cells *in vivo* lies within inter-fibre spaces as depicted
12 in Figure 1(a) (2).
13
14
15
16
17
18
19
20
21
22
23
24
25
26
27

28 In this study, it is proposed that the deposition of fibrin at early time points, either as the
29 result of physiological processes or clinical application, would facilitate cell attachment in inter-
30 fibre regions. This hypothesis was investigated using *in vitro* cultures of human osteoblasts
31 (HObS). The effect of fibrinogen concentration on the cell responses, in terms of morphology,
32 proliferation and metabolic activity, were considered with a focus on physiological levels as the
33 study aimed to create an *in vitro* model of the clinical application of these fibre networks as an *in*
34 *vivo* implant coating.
35
36
37
38
39
40
41
42
43
44

45 The network employed contains 17 vol% of 444 ferritic stainless steel fibres. As
46 illustrated in Figure 2(a), the inter-fibre spaces are of the order of 400-500 μm , which are
47 considered suitable for allowing the ingress of cells and nutrients and subsequent vascularization
48 during bone formation (49). The network architecture and fibre volume fraction are important
49 parameters because they affect the spatial distribution of the fibrin within the network.
50 Architecture is also important for the network-mediated cellular responses and subsequent bone
51
52
53
54
55
56
57
58
59
60

1
2
3 formation. Architecture characterisation showed that the majority of the fibres are lying in-plane
4
5 (Table III). In addition, the mean segment length (distance between the joints) was estimated to
6
7 be $425 \mu\text{m} (\pm 6)$, as shown in Table III. Using the equivalent fibre diameter based on the fibre
8
9 cross-sectional area ($80 \times 100 \mu\text{m}^2$), it follows that the fibre segment aspect ratio
10
11 (length/diameter) is ~ 4.25 .[†] Such a value for the fibre segment aspect ratio is relatively low,
12
13 ideally, higher aspect ratio values are desirable as Figure 1(b) shows that networks with
14
15 relatively high fibre segment aspect ratios (>10) would be more readily deformable by the
16
17 application of a magnetic field.
18
19
20
21
22

23 The in-plane Young's moduli of the 83% porous networks are a few GPa (~ 5 GPa),
24
25 suggesting that the networks have moduli in the same range as other porous metallic coatings
26
27 used commercially in prosthetic implants. For example, RegenerexTM (Biomet), which is a
28
29 titanium coating, has a stiffness of ~ 1.6 GPa with 67% porosity (50, 51) whereas Trabecular
30
31 MetalTM (Zimmer), which is made of porous tantalum, has a Young's modulus of ~ 3 GPa with
32
33 porosity of 75-85% (50, 52). In the case of the fibre networks, it is important to note that the
34
35 stiffness of the fibre material, the fibre volume fraction, the fibre orientation distribution and the
36
37 fibre segment aspect ratio are relevant to the magnitude of the Young's modulus values. For
38
39 instance, the through-thickness Young's modulus of these networks is expected to be
40
41 significantly lower due to the fact the fibres are lying in-plane and therefore would offer very
42
43 low resistance to vertical displacement. Also, a higher fibre segment aspect ratio, which is
44
45 desirable for generating high strains to in-growing bone tissue, would make the networks more
46
47
48
49
50
51
52

53
54
55
56 [†] The effective segment aspect ratio may be slightly higher than 4.25 due to section effects. The
57
58 fibres have a non-uniform cross-sectional shape ($80 \times 100 \mu\text{m}^2$), so in practice they would bend in planes
59
60 in which they have relatively low moments of inertia.

1
2
3 readily deformable, resulting in a decrease in stiffness. The corollary is that if a network of this
4 type is to be employed for such an application, all these parameters need to be controlled and
5
6 optimised.
7
8
9

10
11 The cell culture studies were designed in consideration of the *in vivo* conditions for
12 application of the fibre network as an orthopaedic implant coating. In keeping with this
13 approach, one side of the networks was exposed to fibrin and cell attachment as the opposite side
14 would be sintered to the [prosthesis surface](#). Consistent with an *in vitro* model of acute
15 inflammatory responses, fibrin deposition was carried out prior to HOB infiltration. The study
16 compares fibrin deposition from physiological fibrinogen concentrations between 1.5 and 5 g L⁻¹
17 ((35-37)) as an *in vitro* model of *in vivo* inflammatory responses. A supra-physiological (10 g L⁻¹
18
19
20
21
22
23
24
25
26
27
28
29
30
31
32
33
34
35
36
37
38
39
40
41
42
43
44
45
46
47
48
49
50
51
52
53
54
55
56
57
58
59
60
1) concentration was also included as the majority of studies on this topic have focused on
concentrations higher than 5 g L⁻¹ (38, 39). Deposition of fibrin, with similar nanometre scale
diameters, was observed throughout the thickness of the fibre networks in both SEM and CLSM
images (Figures 5 and 6). The general observation of [decreased](#) nanofibre pore sizes agreed well
with the literature reports on fibrin deposition (41).

Cell attachment of HOBs was observed over the surface of the fibre networks and within
inter-fibre spaces in both [CLSM](#) and SEM images (Figures 5 and 6). [Cell proliferation was](#)
[evident between days 1 and 7 for all samples. However, while the cells in the fibrin-containing](#)
[samples proliferated between the fibres \(Figure 5 \(b-d\),\(f-h\),\(j-l\),\(n-p\)\), without fibrin, HOB](#)
[attachment and proliferation was confined to the metal surfaces \(Figure 5 \(a, e, i, m\)\). Cell](#)
[attachment was similar for all fibrinogen concentrations, qualitatively observed by CLSM. For](#)
all time-points and fibrin-containing samples, HOBs attached onto the fibrin and metal fibres,
spreading into morphologies typical of osteoblasts cultured *in vitro*, with numerous cytoplasmic

1
2
3 projections visible at high magnifications (Figures 6 (f)-(h)). In contrast, cell attachment in
4 control samples was confined to the surface of the metal fibres and junctions as the HObs
5 required the support of the underlying metal fibres (Figures 6(a) and 6(e)).
6
7
8
9

10
11 The effects of fibrin deposition on the ability of HObs to proliferate and metabolise
12 within the fibre networks were dependent on concentration and culture time. Cells on scaffolds
13 with supra-physiological fibrinogen concentrations had similar metabolic activities than those
14 with physiological concentrations despite significantly higher cell numbers. These results
15 support earlier reports (38, 39, 41) of decreasing cell activities with increasing fibrinogen
16 concentrations. Considering physiological concentrations, the higher fibrinogen concentration (5
17 g L⁻¹) resulted in significantly higher cell numbers with a similar significant increase in
18 metabolic activities. The lower fibrinogen concentration (3 g L⁻¹) resulted in greater cell
19 metabolic activity to control samples of similar cell numbers. Generally, increased fibrin
20 deposition contributed to increased cell numbers but decreased cell metabolic activities. A
21 potential explanation for this inverse relationship between cell activity and fibrinogen
22 concentration could be the decreased pore sizes in supra-physiological concentrations as
23 suggested in a previous study (41). As indicated in (41), this inverse relationship could contribute
24 to inhibition of medium and nutrient transfer to cells within the fibrin. This hypothesis provides
25 the foundation for further studies in this area.
26
27
28
29
30
31
32
33
34
35
36
37
38
39
40
41
42
43
44
45
46
47

48 **6. Conclusions**

49
50
51 The results of the current study demonstrate that deposition of fibrin nanofibres significantly
52 affects the responses of human osteoblasts seeded into porous fibre networks composed of 444
53 ferritic stainless steel. Such “magneto-active” networks have been proposed as surface layers on
54
55
56
57
58
59
60

1
2
3 prosthetic implants. The local fibre orientations and other architectural characteristics such as the
4
5 fibre segment lengths were measured using X-ray nano-tomography. The measured Young's
6
7 moduli were independent of the in-plane direction suggesting that the network exhibits
8
9 transverse isotropy. In terms of magnitude, the stiffness values were comparable with those of
10
11 porous metallic coatings used commercially.
12
13
14
15

16 Attachment of human osteoblasts was observed over the fibre surfaces and within the
17
18 inter-fibre spaces in fibrin-containing networks. Fibrin deposition influenced the seeding and
19
20 metabolic activity of human osteoblasts in a concentration-dependant manner. While seeding
21
22 efficiency increased with fibrinogen concentration, cell metabolic activities decreased,
23
24 suggesting a negative correlation between cell viability and fibrinogen concentration. The results
25
26 recommend physiological fibrinogen concentrations for promoting early cell attachment within
27
28 the inter-fibre spaces of porous implant coatings.
29
30
31
32
33

34 **Acknowledgements**

35
36
37 This research was supported by the European Research Council (Grant No. 240446).
38
39 Financial support for RAB was provided via the National Institute for Health Research. The
40
41 authors would like to thank Ms Anne Bahnweg for assistance with SEM and Dr Jeremy Skepper
42
43 for assistance with CLSM.
44
45
46
47

48 **Author Disclosure Statement**

49
50
51 No competing financial interests exist.
52
53
54
55
56
57
58
59
60

References

1. Markaki, A.E., and Clyne, T.W. Magneto-Mechanical Actuation of Bonded Ferromagnetic Fibre Arrays. *Acta Materialia* **53**, 877, 2005.
2. Markaki, A.E., and Clyne, T.W. Magneto-Mechanical Stimulation of Bone Growth in a Bonded Array of Ferromagnetic Fibres. *Biomaterials* **25**, 4805, 2004.
3. Elster, A.D., and Burdette, J.H. *Questions & Answers in Magnetic Resonance Imaging*. 2 ed. St. Louis: Mosby; 2001.
4. Tegawa, Y., and Kinouchi, Y. Dental magnetic attachment: Toward third generation devices. *Ieee Transactions on Biomedical Engineering* **55**, 1185, 2008.
5. Nakamura, K., Takada, Y., Yoda, M., Kimura, K., and Okuno, O. Galvanic corrosion of ferritic stainless steels used for dental magnetic attachments in contact with an iron-platinum magnet. *Dental Materials Journal* **27**, 203, 2008.
6. Dowling, N.J.E., Kim, Y.H., Ahn, S.K., and Lee, Y.D. Effect of alloying elements and residuals on corrosion resistance of type 444 stainless steel. *Corrosion* **55**, 187, 1999.
7. Asami, K., and Hashimoto, K. Importance of initial surface film in the degradation of stainless steels by atmospheric exposure. *Corrosion Science* **45**, 2263, 2003.
8. Malheiro, V.N., Spear, R.L., Brooks, R.A., and Markaki, A.E. Osteoblast and monocyte responses to 444 ferritic stainless steel intended for a Magneto-Mechanically Actuated Fibrous Scaffold. *Biomaterials* **32**, 6883, 2011.
9. Malheiro, V.N., Skepper, J.N., Brooks, R.A., and Markaki, A.E. In vitro osteoblast response to ferritic stainless steel fiber networks for magneto-active layers on implants. *J Biomed Mater Res Part A* **101A**, 1588, 2013.
10. Symeonidou, A., Spear, R.L., Brooks, R.A., and Markaki, A.E. Human Mesenchymal Stem Cell Response to 444 Ferritic Stainless Steel Networks. *MRS Proceedings* **1569**, 2013.
11. Spear, R.L., Brooks, R.A., and Markaki, A.E. Short-term in vitro responses of human peripheral blood monocytes to ferritic stainless steel fiber networks. *J Biomed Mater Res Part A* **101A**, 1456, 2013.
12. Isaksson, H., van Donkelaar, C.C., and Ito, K. Sensitivity of tissue differentiation and bone healing predictions to tissue properties. *Journal of Biomechanics* **42**, 555, 2009.
13. Frost, H.M. Bone “mass” and the “mechanostat”: A proposal. *The Anatomical Record* **219**, 1, 1987.
14. Rubin, C.T., and Lanyon, L.E. Regulation of bone mass by mechanical strain magnitude. *Calcif Tissue Int* **37**, 411, 1985.
15. Neelakantan, S., Bosbach, W., Woodhouse, J., and Markaki, A.E. Characterization and deformation response of orthotropic fibre networks with auxetic out-of-plane behaviour. *Acta Materialia* **66**, 326, 2014.
16. Zou, C., Zhang, E., Li, M., and Zeng, S. Preparation, microstructure and mechanical properties of porous titanium sintered by Ti fibres. *J Mater Sci: Mater Med* **19**, 401, 2007.
17. Delannay, F., and Clyne, T.W. Elastic properties of cellular metals processed by sintering mats of fibres. In: Banhart J., Ashby M.F., A F.N., eds. *Met Foam 99*: MIT-Verlag; 1999. pp. 293.
18. Ducheyne, P., Aernoudt, E., and De Meester, P. The mechanical behaviour of porous austenitic stainless steel fibre structures. *J Mater Sci* **13**, 2650, 1978.

19. Jayanty, S., Crowe, J., and Berhan, L. Auxetic fibre networks and their composites. *Physica Status Solidi (b)* **248**, 73, 2011.
20. Clyne, T.W., and Withers, P.J. *An Introduction to Metal Matrix Composites*. Cambridge: Cambridge University Press; 1993.
21. Doolittle, R.F. Fibrinogen and fibrin. *Annual Review of Biochemistry* **53**, 195, 1984.
22. Mosesson, M.W. Fibrinogen and fibrin structure and functions. *Journal of Thrombosis and Haemostasis* **3**, 1894, 2005.
23. Mosesson, M.W., Siebenlist, K.R., and Meh, D.A. The Structure and Biological Features of Fibrinogen and Fibrin. *Annals of the New York Academy of Sciences* **936**, 11, 2001.
24. Ahmed, T.A.E., Dare, E.V., and Hincke, M. Fibrin: A versatile scaffold for tissue engineering applications. *Tissue Engineering Part B-Reviews* **14**, 199, 2008.
25. Jackson, M.R. Fibrin sealants in surgical practice: An overview. *The American Journal of Surgery* **182**, S1, 2001.
26. Wong, C., Inman, E., Spaethe, R., and Helgerson, S. Fibrin-based biomaterials to deliver human growth factors. *Thrombosis and Haemostasis* **89**, 573, 2003.
27. Lei, P., Padmashali, R.M., and Andreadis, S.T. Cell-controlled and spatially arrayed gene delivery from fibrin hydrogels. *Biomaterials* **30**, 3790, 2009.
28. Gorodetsky, R., Clark, R.A.F., An, J.Q., Gailit, J., Levdansky, L., Vexler, A., Berman, E., and Marx, G. Fibrin microbeads as biodegradable carriers for culturing cells and for accelerating wound healing. *Journal of Investigative Dermatology* **112**, 866, 1999.
29. Silverman, R.P., Passaretti, D., Huang, W., Randolph, M.A., and Yaremchuk, M. Injectable tissue-engineered cartilage using a fibrin glue polymer. *Plast Reconstr Surg* **103**, 1809, 1999.
30. Eyrich, D., Brandl, F., Appel, B., Wiese, H., Maier, G., Wenzel, M., Staudenmaier, R., Goepferich, A., and Blunk, T. Long-term stable fibrin gels for cartilage engineering. *Biomaterials* **28**, 55, 2007.
31. Currie, L.J., Sharpe, J.R., and Martin, R. The use of fibrin glue in skin grafts and tissue-engineered skin replacements: A review. *Plast Reconstr Surg* **108**, 1713, 2001.
32. Perka, C., Schultz, O., Spitzer, R.S., Lindenhayn, K., Burmester, G.R., and Sittinger, M. Segmental bone repair by tissue-engineered periosteal cell transplants with bioresorbable fleece and fibrin scaffolds in rabbits. *Biomaterials* **21**, 1145, 2000.
33. Yamada, Y., Boo, J.S., Ozawa, R., Nagsaka, T., Okazaki, Y., Hata, K., and Ueda, M. Bone regeneration following injection of mesenchymal stem cells and fibrin glue with a biodegradable scaffold. *J Cranio-MaxilloFac Surg* **31**, 27, 2003.
34. Gurevich, O., Vexler, A., Marx, G., Prigozhina, T., Levdansky, L., Slavin, S., Shimeliovich, I., and Gorodetsky, R. Fibrin microbeads for isolating and growing bone marrow-derived progenitor cells capable of forming bone tissue. *Tissue Eng* **8**, 661, 2002.
35. Giddings, J.C., and Bloom, A.L. Study of 2 methods for estimating plasma fibrinogen and effect of epsilon aminocaproic acid and protamine. *Journal of Clinical Pathology* **24**, 467, 1971.
36. Arneson, D. Quantitative-analysis of plasma fibrin monomer. *Thrombosis Research* **8**, 31, 1976.
37. Kratz, A., Ferraro, M., Sluss, P.M., and Lewandrowski, K.B. Laboratory reference value. *New England Journal of Medicine* **351**, 1548, 2004.
38. Cox, S., Cole, M., and Tawil, B. Behavior of human dermal fibroblasts in three-dimensional fibrin clots: Dependence on fibrinogen and thrombin concentration. *Tissue Eng* **10**, 942, 2004.

- 1
2
3 39. Ho, W., Tawil, B., Dunn, J.C.Y., and Wu, B.M. The behavior of human mesenchymal stem
4 cells in 3D fibrin clots: Dependence on fibrinogen concentration and clot structure. *Tissue Eng*
5 **12**, 1587, 2006.
- 6
7 40. Barsotti, M.C., Magera, A., Armani, C., Chiellini, F., Felice, F., Dinucci, D., Piras, A.M.,
8 Minnocci, A., Solaro, R., Soldani, G., Balbarini, A., and Di Stefano, R. Fibrin acts as biomimetic
9 niche inducing both differentiation and stem cell marker expression of early human endothelial
10 progenitor cells. *Cell Prolif* **44**, 33, 2011.
- 11
12 41. Vavken, P., Joshi, S.M., and Murray, M.M. Fibrin concentration affects ACL fibroblast
13 proliferation and collagen synthesis. *Knee* **18**, 42, 2011.
- 14
15 42. Colley, H., McArthur, S.L., Stolzing, A., and Scutt, A. Culture on fibrin matrices maintains
16 the colony-forming capacity and osteoblastic differentiation of mesenchymal stem cells. *Biomed*
17 *Mater* **7**2012.
- 18
19 43. Tsarouchas, D., and Markaki, A.E. Extraction of fibre network architecture by X-ray
20 tomography and prediction of elastic properties using an affine analytical model. *Acta Materialia*
21 **59**, 6989, 2011.
- 22
23 44. Oh, W., and Lindquist, W.B. Image thresholding by indicator kriging. *IEEE Trans Pattern*
24 *Anal Mach Intell* **21**, 590, 1999.
- 25
26 45. WB, L. 3DMA General Users Manual. New York: State University of New York at Stony
27 Brook; 1999.
- 28
29 46. Yang, H. A geometric and statistical analysis of fibrous materials from three-dimensional
30 high resolution images. Doctor of Philosophy. Applied Mathematics and Statistics, State
31 University of New York at Stony Brook, Stony Brook, USA, May 2001.
- 32
33 47. McIntyre, M.E., and Woodhouse, J. On measuring the elastic and damping constants of
34 orthotropic sheet materials. *Acta Metallurgica* **36**, 1397, 1988.
- 35
36 48. AlamarBlue™ Technical Datasheet. AbD Serotec Ltd; 2002.
- 37
38 49. Karageorgiou, V., and Kaplan, D. Porosity of 3D biomaterial scaffolds and osteogenesis.
39 *Biomaterials* **26**, 5474, 2005.
- 40
41 50. Levine, B. A New Era in Porous Metals: Applications in Orthopaedics. *Advanced*
42 *Engineering Materials* **10**, 788, 2008.
- 43
44 51. Lombardi, A.V., Jr., Berasi, C.C., and Berend, K.R. Evolution of tibial fixation in total knee
45 arthroplasty. *Journal of Arthroplasty* **22**, 25, 2007.
- 46
47
48
49
50
51
52
53
54
55
56
57
58
59
60

1
2
3
4
5
6
7
8
9
10
11
12
13
14
15
16
17
18
19
20
21
22
23
24
25
26
27
28
29
30
31
32
33
34
35
36
37
38
39
40
41
42
43
44
45
46
47
48
49
50
51
52
53
54
55
56
57
58
59
60

For Peer Review ONLY! Not for Distribution

Figure legends

Figure 1. (a) A schematic representation of how a ferromagnetic fibre network would deform in a magnetic field B ; (b) Predicted dependence of the peak strain generated within surrounding tissue as a function of the fibre segment aspect ratio on applying a magnetic field of 1 Tesla to a ferromagnetic fibre network.

Figure 2. Representative SEM images showing: (a) top view of a 444 stainless steel fibre network; (b) surface morphology of 444 ferritic stainless steel fibres, and (c) top view of a fibre network after 1 day of cell culture with human osteoblasts.

Figure 3. (a) A three-dimensional tomographic visualisation ($4 \times 4 \times 2 \text{ mm}^3$) of the 444 network; (b) The medial axes network and reconstructed fibres; (c) Probability distribution of fibre segment inclination angle θ to the through thickness direction ($n = 2$).

Figure 4. Optical (a-d) and SEM images (e-h) showing top view of stainless steel fibre networks following fibrin deposition from (left-right) 0, 3, 5 and 10 g L⁻¹ fibrinogen solutions after 1 day in culture. Insert in 4(b) depicts a representative image of networks (white) with fibrin (red) deposited from 3 g L⁻¹ fibrinogen solutions containing 1% fibrinogen-AlexaFluor[®] 594, following 1 day of culture.

1
2
3
4
5
6
7 Figure 5. CLSM images showing top views of stainless steel fibre networks following fibrin
8 deposition from (a, e, i, m) 0 g L^{-1} ; (b, f, j, n) 3 g L^{-1} ; (c, g, k, o) 5 g L^{-1} and (d, h, l, p) 10 g L^{-1}
9 fibrinogen solutions following 1 (a-d, i-l) and 7 (e-h, m-p) days of cell culture. Figures 5 (a-d, e-
10 h) show actin (green, AlexaFluor[®] 488) and nuclei (blue, DAPI). Figures 5 (i-l, m-p) show
11 reflectance from metal fibres.
12
13
14
15
16
17
18
19
20
21

22 Figure 6. SEM images showing top views of stainless steel fibre networks following fibrin
23 deposition from (left-right) 0, 3, 5 and 10 g L^{-1} fibrinogen solutions following 7 days of cell
24 culture.
25
26
27
28
29
30
31
32

33 Figure 7. CyQuant[®] analysis for DNA of HObs seeded onto fibrin-coated fibre networks
34 showing (a) cell number following 1, 3 and 7 days of culture and (b) cell number after 1 day of
35 culture presented as a percent of initial seeding concentration. (c) Metabolic activity of HObs
36 seeded onto fibre networks following fibrin deposition from 0, 3, 5 and 10 g L^{-1} fibrinogen
37 solutions following 1, 3 and 7 days of culture. For CyQuant[®], two-way ANOVA analysis was
38 performed to test for statistical significance followed by Tukey post-hoc analysis; for
39 alamarBlue[®], statistical significance was analysed using Games-Howell post-hoc analysis (Mean
40 \pm SD, $n = 3$) (* indicates statistical difference considering fibrinogen concentrations, $p < 0.05$)
41 Cell number also increased significantly ($p < 0.05$) between day 1 and 7. Seeding efficiency was
42 analysed using Pearson's correlation coefficient ($p < 0.01$).
43
44
45
46
47
48
49
50
51
52
53
54
55
56
57
58
59
60

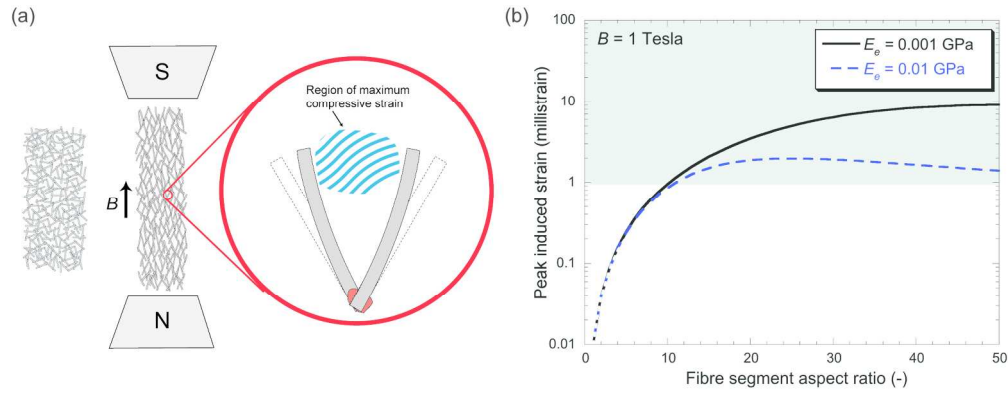


Figure 1
189x73mm (300 x 300 DPI)

1
2
3
4
5
6
7
8
9
10
11
12
13
14
15
16
17
18
19
20
21
22
23
24
25
26
27
28
29
30
31
32
33
34
35
36
37
38
39
40
41
42
43
44
45
46
47
48
49
50
51
52
53
54
55
56
57
58
59
60

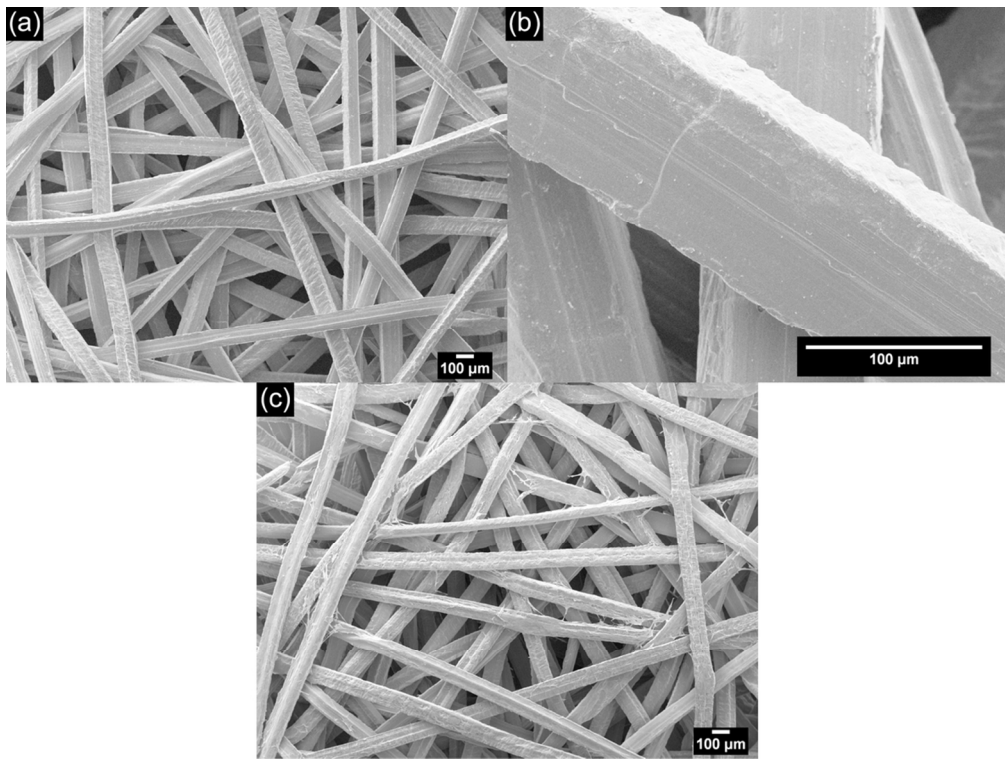


Figure 2
99x75mm (300 x 300 DPI)

Not for Distribution

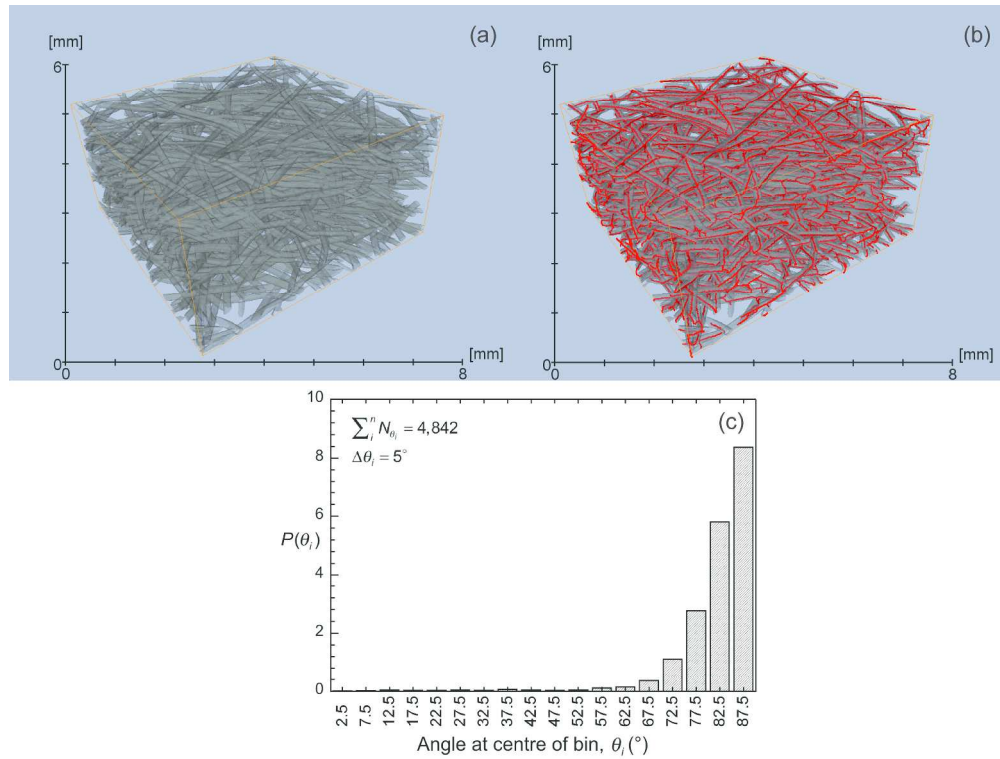


Figure 3
293x224mm (300 x 300 DPI)

1
2
3
4
5
6
7
8
9
10
11
12
13
14
15
16
17
18
19
20
21
22
23
24
25
26
27
28
29
30
31
32
33
34
35
36
37
38
39
40
41
42
43
44
45
46
47
48
49
50
51
52
53
54
55
56
57
58
59
60

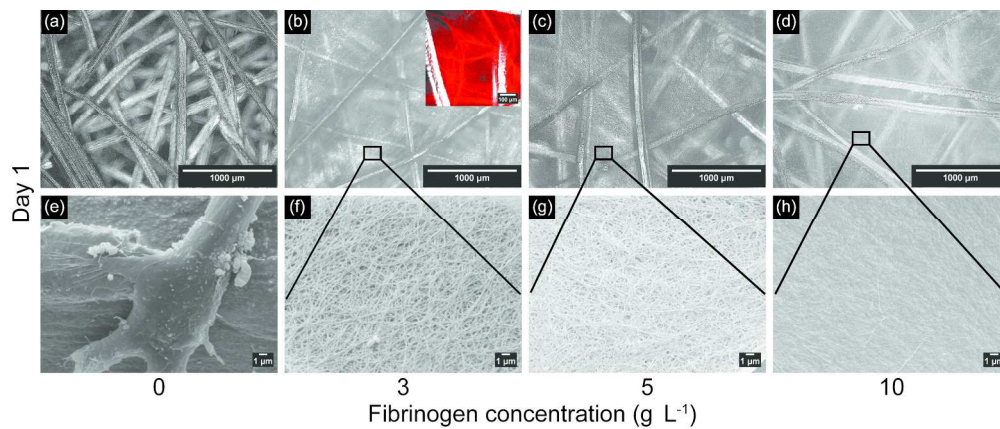


Figure 4
211x88mm (300 x 300 DPI)

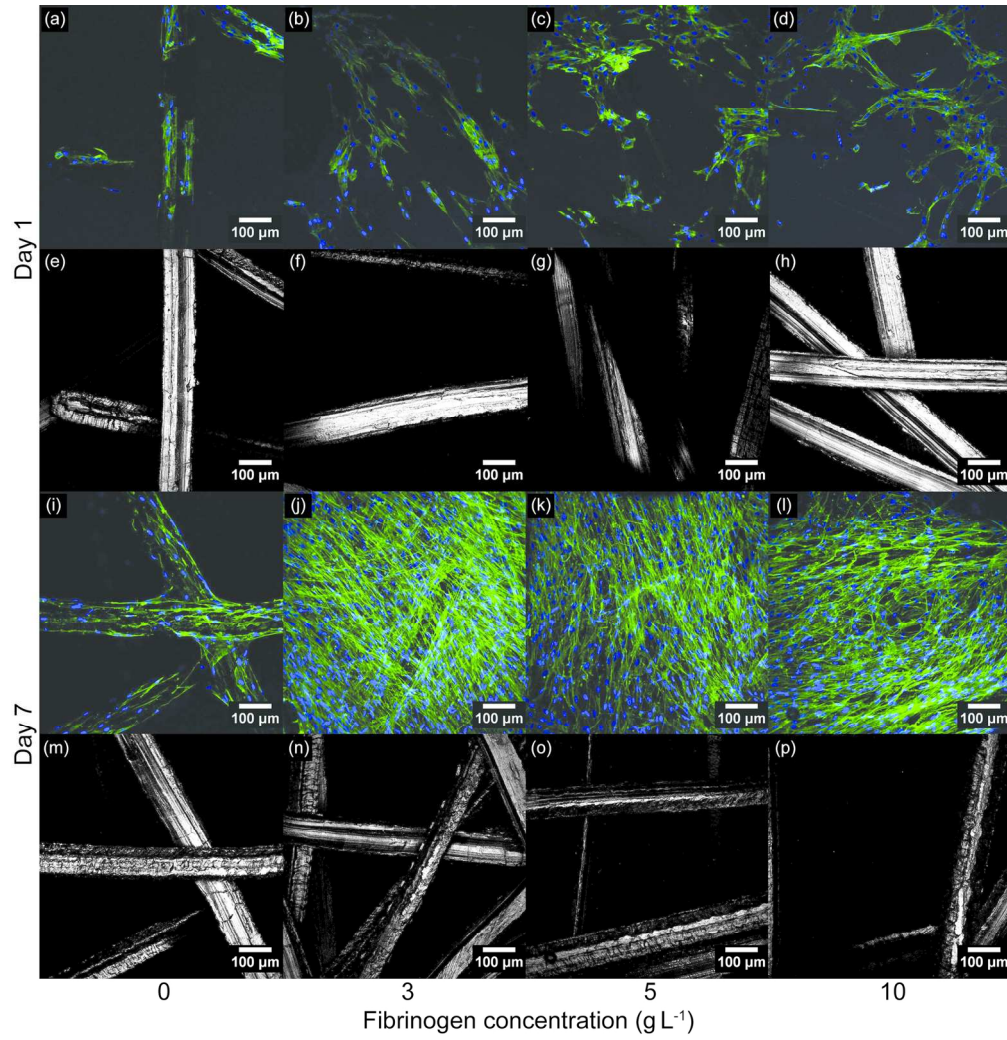


Figure 5
159x164mm (300 x 300 DPI)

1
2
3
4
5
6
7
8
9
10
11
12
13
14
15
16
17
18
19
20
21
22
23
24
25
26
27
28
29
30
31
32
33
34
35
36
37
38
39
40
41
42
43
44
45
46
47
48
49
50
51
52
53
54
55
56
57
58
59
60

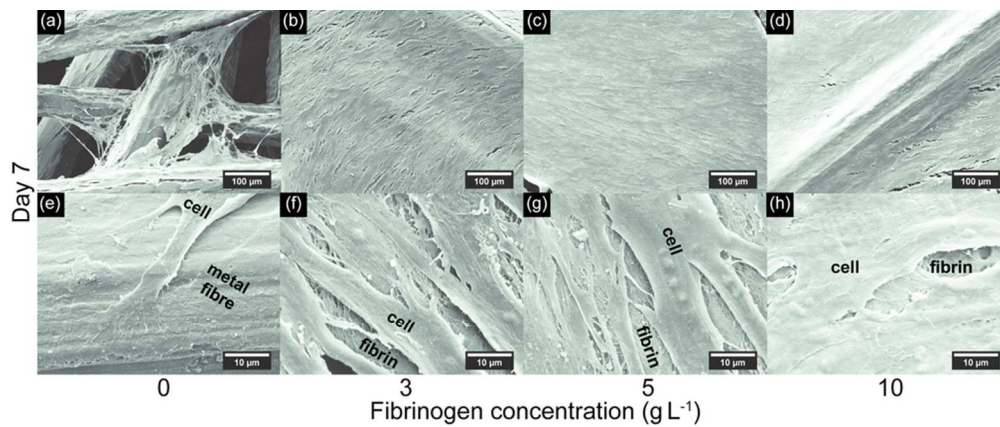


Figure 6
85x35mm (300 x 300 DPI)

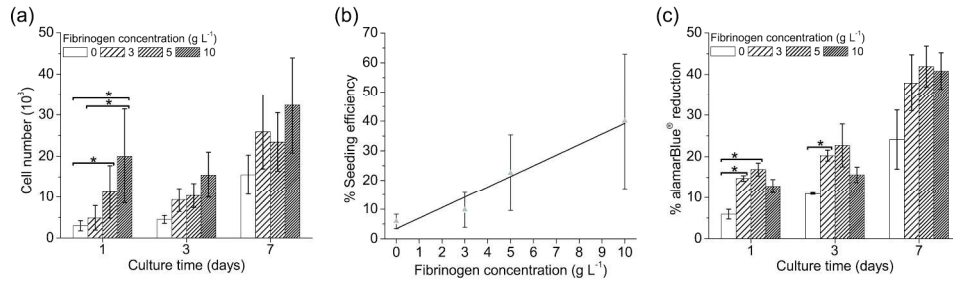


Figure 7
247x71mm (300 x 300 DPI)

| AISI type | Composition, wt % | | | | | | | | | |
|-----------|-------------------|-------|-------|--------|--------|-------------|-----------|--------|-------|---------|
| | C | Mn | Si | P | S | Cr | Mo | N | Ti/Nb | Fe |
| 444 | ≤0.025 | ≤1.00 | ≤1.00 | ≤0.040 | ≤0.015 | 17.00-20.00 | 1.80-2.50 | ≤0.030 | ≤0.45 | balance |

Table I: Chemical composition of AISI 444 steel.

1
2
3
4
5
6
7
8
9
10
11
12
13
14
15
16
17
18
19
20
21
22
23
24
25
26
27
28
29
30
31
32
33
34
35
36
37
38
39
40
41
42
43
44
45
46
47
48
49

Pre-Review ONLY! Not for Distribution

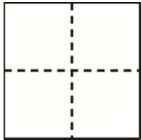
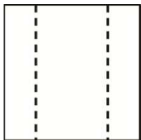
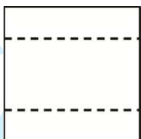
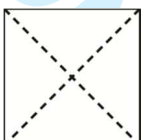
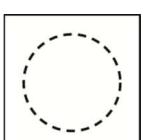
| Mode No. | Mode Shapes | Frequency (Hz) | |
|----------|---|----------------|-----------|
| | | Measured | Predicted |
| 1 |  | 102 | 102 |
| 2 |  | 136 | 135 |
| 3 |  | 227 | 227 |
| 4 |  | 194 | 195 |
| 5 |  | 244 | 244 |

Table II. Measured and predicted mode frequencies (in Hz) for rectangular and square plates of 444 ($80 \times 100 \mu\text{m}^2$) fibre networks.

| Material | Fibre volume fraction (%) [*] | No of fibres (-) | No of fibre segments (-) | Mean segment length (μm) | Mean fibre inclination angle, θ (°) |
|----------|--|------------------|--------------------------|--------------------------|-------------------------------------|
| 444 | 17.1 ± 0.33 | 660 ± 9 | 4707 ± 136 | 425 ± 6 | 82.08 ± 0.25 |

^{*}As determined using the volumetric method (§2.2).

Table III: Network architecture characteristics obtained from X-ray tomography (*n* = 2).

1
2
3
4
5
6
7
8
9
10
11
12
13
14
15
16
17
18
19
20
21
22
23
24
25
26
27
28
29
30
31
32
33
34
35
36
37
38
39
40
41
42
43
44
45
46
47
48
49

Peer Review ONLY! Not for Distribution

| In-plane Elastic Moduli (GPa) | | Poisson's ratios (-) | | Shear Modulus G_{xy} (GPa) |
|----------------------------------|-------|-------------------------|------------|------------------------------------|
| E_x | E_y | ν_{xy} | ν_{yx} | |
| 4.60 | 4.79 | 0.30 | 0.32 | 1.60 |

Table IV. In-plane elastic constants for 444 ($80 \times 100 \mu\text{m}^2$) fibre networks, as measured by plate vibrations.

Supplementary Data

“Physical and biological characterisation of ferromagnetic fibre networks: effect of fibrin deposition on short-term *in vitro* responses of human osteoblasts”

Rose L. Spear¹, Brajith Srigengan¹, Suresh Neelakantan¹, Wolfram Bosbach¹, Roger A.

Brooks² and Athina E. Markaki^{1*}

¹*Department of Engineering, University of Cambridge, Trumpington Street, Cambridge, CB2 1PZ, UK,*

²*Division of Trauma & Orthopaedic Surgery, Addenbrooke's Hospital, Hills Road, Cambridge, CB2 2QQ, UK*

**Corresponding author. TEL.:+44-1223-766417. FAX.:+44-1223-332662. E-mail address:*

am253@cam.ac.uk

Materials and methods

Cell differentiation

Osteogenic differentiation was characterised by alkaline phosphatase (ALP) activity. ALP assay buffer was prepared from glycine (200 mM) in distilled water, adjusted to pH 10.4 with sodium hydroxide (1 M) and supplemented with magnesium chloride hexahydrate (2 mM) and zinc chloride (2 mM). Triplicate aliquots of 50 μ L were removed from each sample lysate, prepared as for the CyQuant® assay, and mixed with 50 μ L of ALP assay buffer containing 6,8-difluoro-4-methylumbelliferyl phosphate (DiFMUP). Samples ($n = 3$) were incubated (15 min, 37°C) to produce the fluorescent compound 6,8-difluoro-7-hydroxy-4-methylcoumarin (DiFMU). ALP activity was measured fluorometrically (excitation 360 nm, emission 455 nm). The emission intensity units of the signal were converted to the amount (nmoles) of DiFMU per 10,000 cells using a DiFMU standard curve.

Results and discussion

Cell differentiation

The activity of alkaline phosphatase, an indicator of osteoblast differentiation, is presented in Figure S1. Low (nmoles per 10^4 cells) amounts of alkaline phosphatase activity were measured for all samples. At day 3, cells cultured on networks containing fibrin deposited from supra-physiological concentrations and high physiological concentrations of fibrinogen had significantly lower alkaline phosphatase activity than the control samples without fibrin.

The low levels of alkaline phosphatase activity for all samples can be attributed to the lack of osteogenic supplements, such as dexamethasone and beta-glycerophosphate, in the growth medium. After three days of culture, cells cultured on networks containing fibrin nanofibres deposited from supra-physiological concentrations resulted in significantly lower HOOb differentiation compared with control samples. These results support earlier reports [38, 39, 41] of decreasing cell activities with increasing fibrinogen concentrations. Considering physiological concentrations, cell cultured on networks containing fibrin deposited from the higher fibrinogen concentration (5 g L^{-1}) had significantly lower differentiation compared with control samples. Generally, increased fibrin deposition contributed to decreased cell activities in terms of differentiation.

Figure legends

Figure S1. Alkaline phosphatase (ALP) activity of HOOb seeded onto fibre networks following fibrin deposition from 0, 3, 5 and 10 g L^{-1} fibrinogen solutions following 1, 3 and 7 days of culture. ALP activity is presented as the amount of DiFMU (nmoles) produced per 10^4 cells after incubation at 37°C for 15 min. Statistical significance was analysed using

1
2
3
4
5
6
7
8
9
10
11
12
13
14
15
16
17
18
19
20
21
22
23
24
25
26
27
28
29
30
31
32
33
34
35
36
37
38
39
40
41
42
43
44
45
46
47
48
49
50
51
52
53
54
55
56
57
58
59
60

Games-Howell post-hoc analysis (Mean \pm SD, $n = 3$). (* indicates statistical difference, $p < 0.05$) considering fibrinogen concentrations.

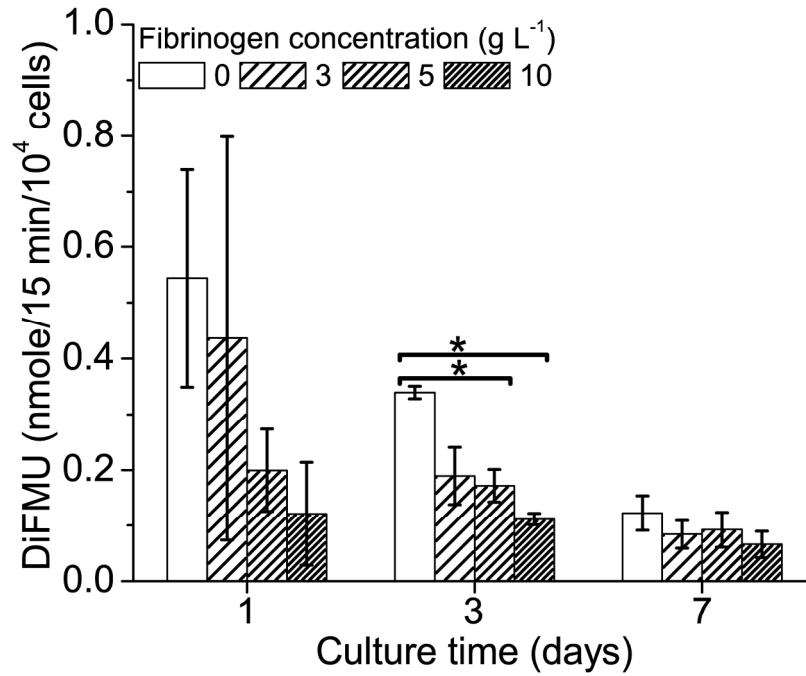


Figure S1
201x156mm (300 x 300 DPI)